

# Corrosion behavior of heat-resistant steel T91 in high-temperature supercritical carbon dioxide with impurity O<sub>2</sub>, SO<sub>2</sub> or H<sub>2</sub>S

Yafei Liu<sup>a,b</sup>, Gang Xiao<sup>a,\*</sup>, Mingxuan Wang<sup>a,b</sup>, Qinghe Guo<sup>a,b</sup>, Zheng Wang<sup>a,b</sup>, Yi Wu<sup>a,b</sup>, Haoran Xu<sup>a,b</sup>, Dong Chen<sup>a,b</sup>

<sup>a</sup> State Key Laboratory of Clean Energy Utilization, Zhejiang University, 38 Zheda Road, Hangzhou 310027, China

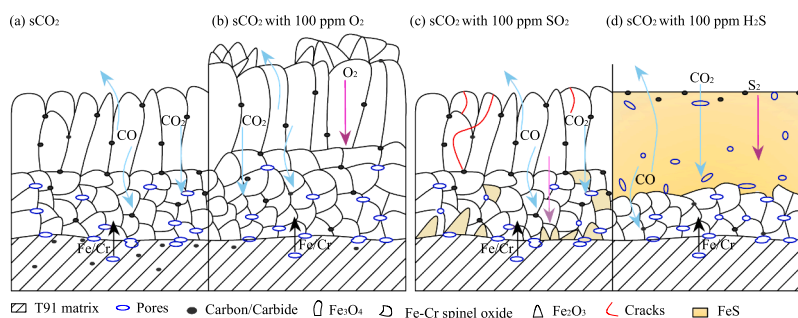
<sup>b</sup> Key Laboratory of Clean Energy and Carbon Neutrality of Zhejiang, Jiaxing Institute of Zhejiang University, 966 Xiuyuan Road, Jiaxing 314031, China

## HIGHLIGHTS

- Addition of O<sub>2</sub> impurity slightly increased mass gain of corroded T91.
- Introduction of SO<sub>2</sub> or H<sub>2</sub>S remarkably exacerbated corrosion of T91 steel with sulfides produced.
- Outer FeS and inner Fe-Cr spinel oxide formed in T91 after exposure to sCO<sub>2</sub> with H<sub>2</sub>S impurity.
- Existence of O<sub>2</sub>, SO<sub>2</sub> or H<sub>2</sub>S reduced carburization of T91.

## GRAPHICAL ABSTRACT

Effects of impurities on corrosion behaviors of T91 steel in four different supercritical carbon dioxide environments at 550 °C and 15 MPa



## ARTICLE INFO

### Keywords:

Supercritical carbon dioxide  
High-temperature corrosion  
Impurities  
Oxides/Sulfides  
Carburization

## ABSTRACT

This study investigated corrosion of T91 in supercritical carbon dioxide (sCO<sub>2</sub>) with impurity of 100 ppm O<sub>2</sub>, SO<sub>2</sub> or H<sub>2</sub>S at 550 °C and 15 MPa. O<sub>2</sub> slightly increased mass gain of corroded T91, and the corrosion kinetics both in pure sCO<sub>2</sub> and in sCO<sub>2</sub> with O<sub>2</sub> impurity followed parabolic law. Fe<sub>2</sub>O<sub>3</sub> was formed in outer corrosion layer due to enhanced partial pressure of oxygen. SO<sub>2</sub> or H<sub>2</sub>S remarkably exacerbated T91 corrosion. For test in sCO<sub>2</sub> with SO<sub>2</sub> impurity, outer corrosion product was magnetite, and the inner was composed of Fe-Cr spinel and FeS, different from that in pure sCO<sub>2</sub>. Addition of H<sub>2</sub>S caused an external FeS layer and internal Fe-Cr spinel. Introduction of all the three impurities reduced carburization in the underlying alloy substrate.

## 1. Introduction

Supercritical carbon dioxide (sCO<sub>2</sub>) Brayton cycle power generation system has been attracting increasing attention in recent decades, because of its simple cycle layout, compact structure and high energy

conversion efficiency [1,2]. In addition, sCO<sub>2</sub> Brayton cycle can be well employed in many energy fields, including nuclear power [3,4], fossil fuels energy [4–6] and concentrated solar power [4,7–9], etc. As an advanced energy conversion system, its technical feasibility has been demonstrated by many institutes across the world, such as Sandia

\* Corresponding author.

E-mail address: [xiaogangtianmen@zju.edu.cn](mailto:xiaogangtianmen@zju.edu.cn) (G. Xiao).

<https://doi.org/10.1016/j.supflu.2023.105936>

Received 2 December 2022; Received in revised form 19 March 2023; Accepted 1 April 2023

Available online 3 April 2023

0896-8446/© 2023 Elsevier B.V. All rights reserved.

**Table 1**  
Chemical compositions of investigated material T91 (in wt%).

Materials	C	Mn	P	S	Cr	Mo	Nb	Ni	Fe	Others
T91	0.047	0.052	0.016	0.007	8.223	0.908	0.075	0.029	Bal.	Si : 0.304 V: 0.210 N : 0.050 Al : 0.010

National Laboratories [10,11], Bechtel Marine Propulsion Corporation [12,13], Nuclear Power institute of China [14,15], etc. sCO<sub>2</sub> Brayton cycle shows great potential to be commercialized in the near future.

However, in the advanced sCO<sub>2</sub> Brayton cycle, the operating temperature and pressure of the key components such as heat exchanger and turbine are at the range of 400–800 °C and 8–30 MPa, respectively [16]. Therefore, the stability of metallic materials exposed to sCO<sub>2</sub> environment at high temperature and high pressure is very essential for the long-term, safe and reliable operation of sCO<sub>2</sub> power generation system. At present, many institutes have conducted experimental investigations on corrosion behaviors of different types of potential steels and alloys used in sCO<sub>2</sub> cycle, such as Korea Advanced Institute of Science and Technology (KAIST), Oak Ridge National Laboratory (ORNL), Xi'an Jiaotong University, etc. Previous studies indicated that metallic materials might cause oxidation and carburization damages when exposed to sCO<sub>2</sub> environment [17,18]. Lee et al. [18] found that a thin and continuous chromia (Cr<sub>2</sub>O<sub>3</sub>) layer was formed on the surface of all investigated alloys (600, 690, 800HT), and they revealed that the carburization resistance was dependent on whether the matrix is Fe-based or Ni-based. They also investigated the effect of temperature and pressure on corrosion behaviors of the three alloys in sCO<sub>2</sub> [19]. Results showed that the corrosion rate increased with increasing temperature, which is in agreement with Ref. [20], and as the test pressure increased from 0.1 MPa to 20 MPa, the extent of an amorphous carbon layer at the oxide/matrix interface increased, consistent with what Bidabadi et al. [21], Pint et al. [22] and Rouillard et al. [23] found. In addition, some key elements like Cr and Ni may seriously affect the corrosion behaviors of metallic materials. Generally, high Cr content can effectively enhance corrosion resistance of steels and alloys, because it is easier to form protective Cr<sub>2</sub>O<sub>3</sub> layer on the metal surface [22,24]. Fe-based alloys with lower Cr content are more likely to form external Fe<sub>3</sub>O<sub>4</sub> and internal Fe-Cr spinel oxidation layers [20–23], which can be explained by void-induced duplex oxide growth model [25–27] or available space model [28]. Chen et al. [29] investigated the corrosion behaviors of four stainless steels with similar Cr content and different Ni content in sCO<sub>2</sub> environment at 650 °C and 20 MPa. They found that Ni element as austenite stabilizer might cause oxide spallation and further exacerbate corrosion damages. Liang et al. [30–33] conducted a series of experiments to investigate the corrosion (oxidation) and carburization of different steels (T91, VM12, Super 304 H, Sanicro 25 and Inconel 617) in high-temperature, high-pressure sCO<sub>2</sub> environment. They proposed a method to determine the dominant process (oxidation or carburization) according to the ratio of C and O elements uptakes, and they also proposed a new defined parameter (corrosion degradation depth) to evaluate the corrosion resistance of heat-resistant steels and alloys. Additionally, internal carburization zones were found underneath the oxide scales, and VM12 showed a high amount of carburization (two orders of magnitude higher than Sanicro 25 and Inconel 617). Gheno et al. [34] proposed an effective thermodynamic model to describe carburization behavior of Fe–9%Cr alloys based on the equilibrium calculation, and Young et al. [35] found that carbon penetrated corrosion layer via oxide grain boundaries using an atom probe analysis method. A model was proposed by Young et al. [36] to describe the non-steady state carburization kinetics of martensitic 9–12%Cr steels in CO<sub>2</sub> rich gases at 550 °C. More relevant findings can be found in a comparative reference [37].

It should be pointed out that most of the interesting findings above are based on corrosion tests in pure sCO<sub>2</sub> (>99.999%) environment. More efforts should be devoted to exploring the impact of impurities on

corrosion of potential steels and alloys, because the CO<sub>2</sub> used for industry always contains certain amounts of aggressive impurities, such as H<sub>2</sub>O, O<sub>2</sub>, H<sub>2</sub>S, SO<sub>2</sub> etc., depending on CO<sub>2</sub> sources and the capture/separation technologies employed. Impurities may exacerbate the corrosion process and even change the corrosion process in sCO<sub>2</sub> environment. For example, Mahaffey et al. [38,39] found that introduction of 10 and 100 ppm O<sub>2</sub> impurity in sCO<sub>2</sub> environment noticeably enhanced oxidation of Ni-based alloy Haynes 230 and 625 with the evidence of oxide spallation and nodule formation. On the contrary, Li et al. [40] concluded that presence of 100 ppm O<sub>2</sub> could improve the Cr<sub>2</sub>O<sub>3</sub> layer stability formed on the surface of austenite stainless steel 310, Ni-based alloy 740 and inhibit the nodule formation. For Fe-based alloys with low Cr concentration, the presence of SO<sub>2</sub> led to a decreased extent of carburization for Fe-9%Cr steels but did not significantly affect the oxidation rate [41], and the existence of H<sub>2</sub>O lowered the carbon activity, probably by partially excluding the carbonaceous species from the oxide scale [42]. Chandra et al. [43] found that oxidation rate of T92 is substantially increased when H<sub>2</sub>O is added to the oxyfuel environment, which was attributed to molecular gas transport. Oleksak et al. [44–46] carried out systematic experimental studies on oxidation and carburization behavior of Fe-based steels in CO<sub>2</sub> containing impurities, and they found that SO<sub>2</sub> with additional H<sub>2</sub>O and O<sub>2</sub> impurities exhibited little effect on oxidation from 550 °C to 600 °C and was likewise beneficial in limiting carburization at lower temperatures. Up to now, investigations on the effects of different impurities on corrosion performance of steels and alloys in high-temperature and high-pressure sCO<sub>2</sub> are limited, especially for impurities with sulfur element like SO<sub>2</sub> and H<sub>2</sub>S. And the findings mentioned above are controversial in some aspects. Therefore, more studies are needed for better understanding of the effects of impurities on corrosion of metallic materials and for better development of materials selection strategy and impurities control standards.

Therefore, in this study, we investigated the corrosion behaviors of heat-resistant steel T91 at 550 °C and 15 MPa for up to 500 h of exposure to sCO<sub>2</sub> environments with 100 ppm O<sub>2</sub>, H<sub>2</sub>S or SO<sub>2</sub> impurity, respectively. Corrosion data was obtained through corrosion mass gain measurement. After exposure, X-ray diffraction (XRD), Scanning Electron Microscopy (SEM) and Energy Dispersive Spectroscopy (EDS) were used to analyze the morphology, chemical compositions and structure of corrosion products.

## 2. Experimental details

### 2.1. Test sample preparation

Experimental material T91 is a potential candidate used in sCO<sub>2</sub> Brayton cycle system, which has been widely employed in superheater, reheater and main steam pipes in coal-fired power plants, because of its good thermal strength, excellent machine-ability and superior economy. The chemical compositions of T91 are shown in Table 1.

Test samples were made from rod-shaped base material by wire cutting method. The dimension of fabricated samples is 20mm × 10mm × 2mm with a hole of 4 mm diameter in the upper middle for suspension. Before exposure, all samples were grounded to 1000 grit surface finish. All polished samples were ultrasonically cleaned in deionized water, ethanol and acetone for 5 min to remove surface impurities and then dried using a drying oven. After that, samples were respectively dimensioned and weighted to obtain surface area and mass using a micrometer and electronic balance before corrosion testing.

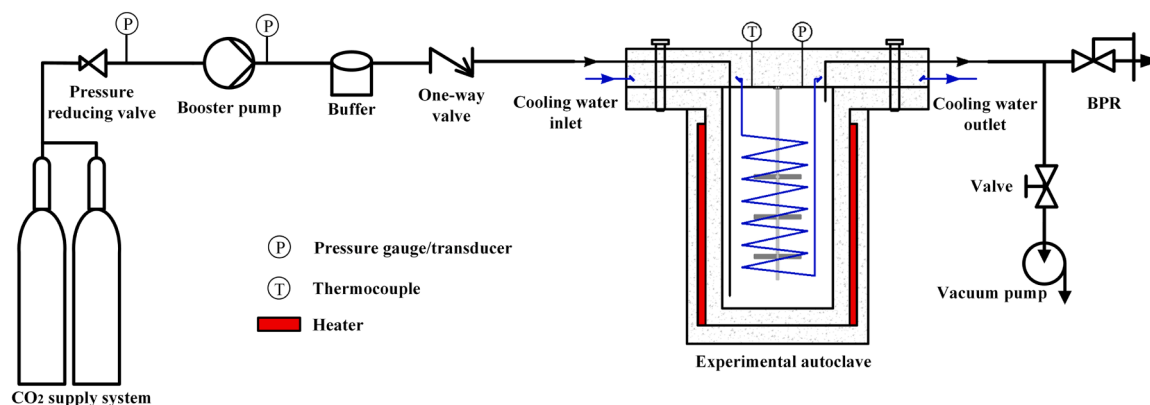


Fig. 1. Corrosion test platform in  $s\text{CO}_2$  at high temperature and high pressure.

## 2.2. Corrosion gas environments

To identify the influence on corrosion of impurity  $\text{O}_2$ ,  $\text{SO}_2$  and  $\text{H}_2\text{S}$  in  $s\text{CO}_2$  environments, four tests were conducted: (1) corrosion in pure  $s\text{CO}_2$  (99.999%), (2) corrosion in pure  $s\text{CO}_2$  with 100 ppm  $\text{O}_2$  impurity, (3) corrosion in pure  $s\text{CO}_2$  with 100 ppm  $\text{SO}_2$  impurity, (4) corrosion in pure  $s\text{CO}_2$  with 100 ppm  $\text{H}_2\text{S}$  impurity.

$\text{CO}_2$  gas mixtures containing 100 ppm  $\text{O}_2$ , 100 ppm  $\text{H}_2\text{S}$  or 100 ppm  $\text{SO}_2$  were carefully prepared using pure  $\text{CO}_2$  with addition of high-purity  $\text{O}_2$  (99.9%),  $\text{H}_2\text{S}$  (99%), and  $\text{SO}_2$  (99.5%), respectively. Firstly, a gas cylinder with a volume of 40 L was vacuumized to  $-0.1$  MPa. Secondly, the density of  $\text{O}_2$ ,  $\text{SO}_2$  or  $\text{H}_2\text{S}$  was obtained according to the ambient temperature and saturated vapor pressure, and then a calculated volume of the impurity was charged into the vacuumized gas cylinder. After that, pure  $\text{CO}_2$  was purged into the gas cylinder until the pressure reached its saturated vapor pressure. Finally, the concentration of impurity was determined using a gas analyzer (WOST-T1800). When the detected concentration of impurity  $\text{O}_2$ ,  $\text{SO}_2$  or  $\text{H}_2\text{S}$  was at the range of 80–120 ppm, the prepared  $\text{CO}_2$  gas mixtures would be used in our

corrosion experiments. Moreover, electric heat tracing was used to improve the homogeneity of gas mixture in the cylinder.

## 2.3. Corrosion experiments

Corrosion experiments were carried out using the  $s\text{CO}_2$  corrosion platform. The schematic of the corrosion test platform is shown in Fig. 1. The test facility mainly includes a  $\text{CO}_2$  supply system, a  $\text{CO}_2$  booster pump, an experimental autoclave, a heater, a cooling water system, a back pressure regulator (BPR) and a vacuum pump. It is worth mentioning that pressurization system is composed of a booster pump, an air compressor and an electromagnetic valve, which can achieve automatic supply of corrosion gas into the experimental autoclave when its pressure is lower than a certain value. Also, it works in coordination with BPR to control the pressure of the autoclave at the range of  $15 \pm 0.2$  MPa. For our corrosion test system, the average gas supply interval was about 40 min at  $550 \pm 1$  °C and  $15 \pm 0.2$  MPa so that the  $s\text{CO}_2$  in autoclave can be refreshed about every 30 h.

For each test, the exposure time was lasted up to 500 h, and the

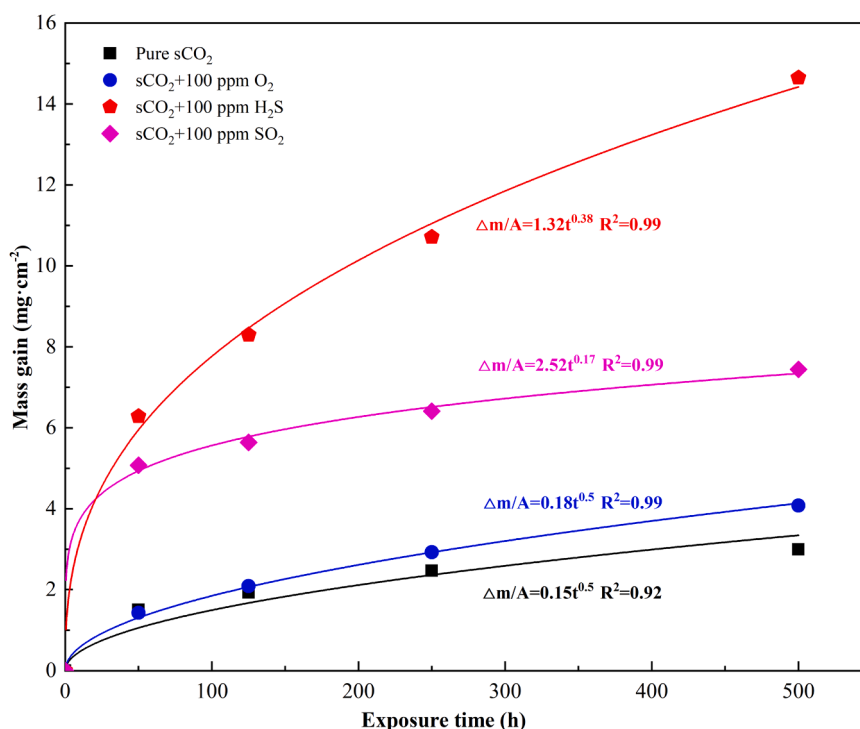


Fig. 2. Mass gains and kinetic curves of T91 exposed to different  $s\text{CO}_2$  environments up to 500 h at 550 °C and 15 MPa.

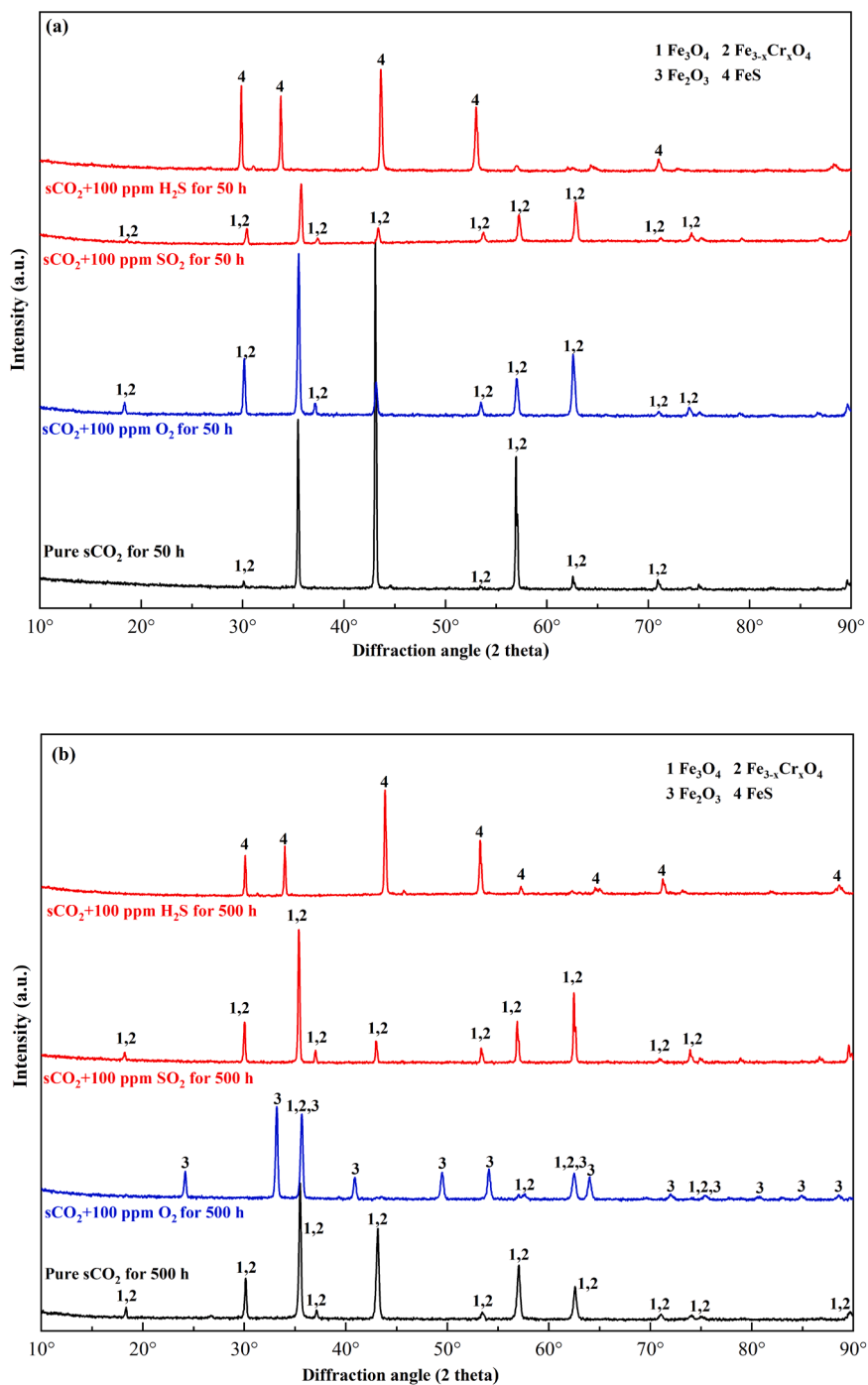


Fig. 3. XRD analysis results of T91 exposed to different sCO<sub>2</sub> environments for (a) 50 h and (b) 500 h of exposure at 550 °C and 15 MPa.

interval periods were chosen to be 50 h, 75 h, 125 h and 250 h. To improve the accuracy of corrosion tests, three replicate specimens for each corrosion period were prepared. After test sample preparation process, freshly prepared specimens were hung on three disc-shaped hangers, and then the autoclave was sealed. Prior to corrosion testing, the residual air in the corrosion system were removed by alternatively vacuuming and purging the pure CO<sub>2</sub> with/without impurity O<sub>2</sub>, H<sub>2</sub>S or SO<sub>2</sub> for three times. Then pure CO<sub>2</sub> or a certified CO<sub>2</sub> mixture was purged into the autoclave. After that, the experimental autoclave was heated up to 550 °C. During the heating period, the autoclave pressure was charged up to ~15 MPa in stages to ensure that the corrosion conditions of 550 °C and 15 MPa were simultaneously achieved and also to enhance the temperature uniformity in the autoclave. At the end of

each designed exposure period, the autoclave was powered off and cooled down to room temperature, and then three corroded samples after a certain exposure period were removed for characterizations.

#### 2.4. Corrosion product characterizations

After every period of the corrosion test, the mass gains of the corroded specimens were measured using a JJ224BC balance with a resolution of 10<sup>-4</sup> g, and then the mass gain per unit area of each corroded sample was calculated. The specimen with the mass gain closest to the average value from three replicates was chosen for further characterizations. X-ray diffractometer (XRD model X-pert powder) was employed to detect the corrosion product phases formed on material

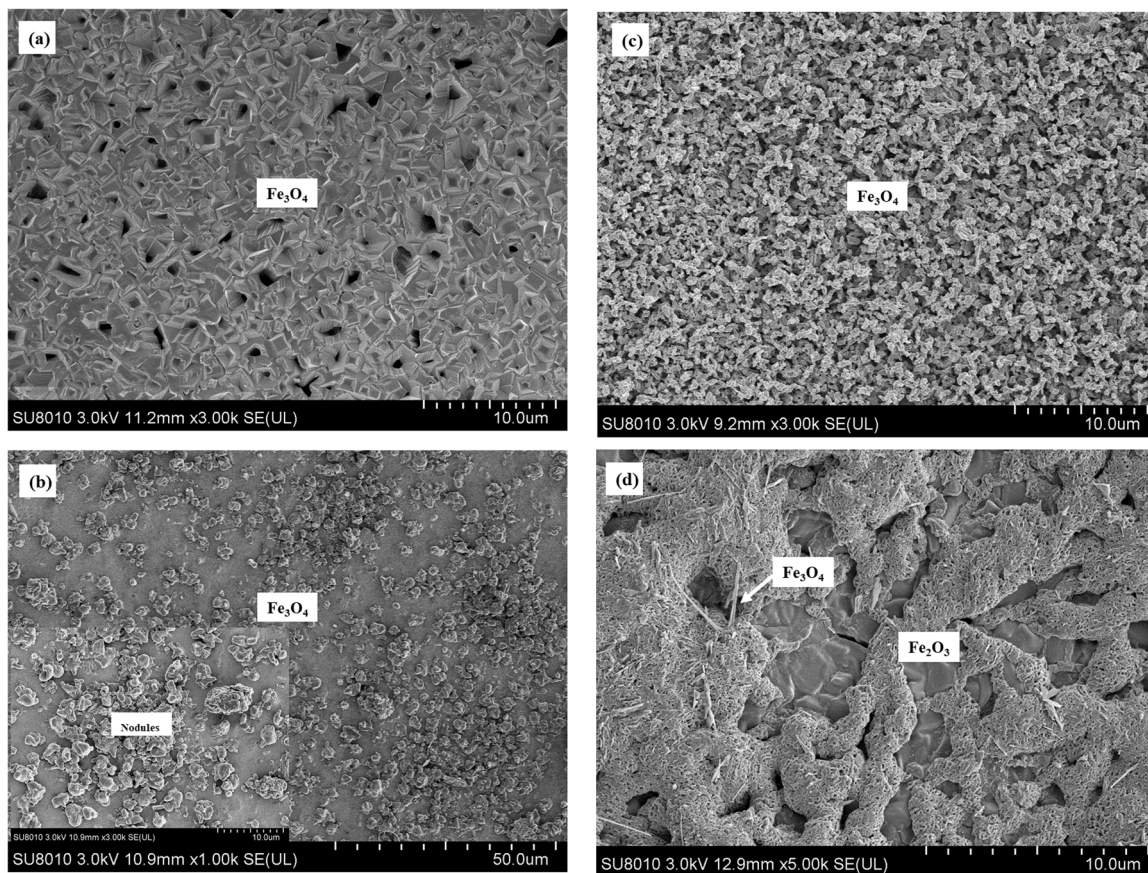


Fig. 4. Surface SEM images of T91 exposed to pure  $s\text{CO}_2$  for (a) 50 h and (b) 500 h, and to  $s\text{CO}_2$  with 100 ppm  $\text{O}_2$  for (c) 50 h and (d) 500 h at 550 °C and 15 MPa.

surfaces. The surface and cross-sectional morphology of the corroded samples were performed using field emission scanning electron microscopy (FE-SEM model SU8010). The elements distributions on specimen surfaces and cross sections were determined by an energy dispersive spectrometer (EDS model Oxford X-max80).

### 3. Results and discussions

#### 3.1. Mass gains and corrosion kinetics

The mass gains of metals in high temperature can be fitted by oxidation laws [40,47], shown in Eq. (1).

$$\frac{\Delta m}{A} = kt^n \quad (1)$$

Where,  $\frac{\Delta m}{A}$  represents the mass gain per unit area during corrosion time.  $k$  is the oxidation constant, and  $n$  is the reaction order.

Mass gains and fitted kinetic curves of the investigated material after corrosion tests in four different  $s\text{CO}_2$  environments at 550 °C and 15 MPa are shown in Fig. 2. The addition of 100 ppm  $\text{H}_2\text{S}$  obviously increased the mass gains of the experimental alloys during exposure periods. After 500 h exposure, the obtained mass gains were respectively increased to  $\sim 2.5$  and  $\sim 4.9$  times with the addition of  $\text{SO}_2$  and  $\text{H}_2\text{S}$  impurity when compared to that in pure  $s\text{CO}_2$  environment. In contrast, the effect of  $\text{O}_2$  impurity on corrosion mass changes was slighter. Furthermore, according to the findings that the mass gain was hardly affected by the presence of  $\text{SO}_2$  with additional impurities  $\text{H}_2\text{O}$  and  $\text{O}_2$  in Refer [44,45], we can conclude that the negative effects of  $\text{SO}_2$  impurity were more pronounced when impurities  $\text{H}_2\text{O}$  and  $\text{O}_2$  were absent, and the influence of  $\text{H}_2\text{S}$  was greater than that of  $\text{SO}_2$ . Additionally, we can also find that the test pressure for corrosion environments with

impurities such as  $\text{H}_2\text{O}$  or  $\text{O}_2$  exhibited little effect on corrosion behavior of Fe-base materials with low Cr content, but improved experiment temperature remarkably deteriorated material corrosion [44].

T91 exhibited a near parabolic behavior with  $n \approx 0.5$  in pure  $s\text{CO}_2$  and with the addition of  $\text{O}_2$  impurity, indicating that the oxidation process was controlled by ion diffusion [20,47]. While the investigated material showed lower corrosion reaction orders with the addition of  $\text{SO}_2$  ( $n \approx 0.17$ ) and  $\text{H}_2\text{S}$  ( $n \approx 0.38$ ) impurity, but higher  $k$  values, implying that the addition of  $\text{SO}_2$  or  $\text{H}_2\text{S}$  impurity might change the corrosion process of T91 as a result of an accelerated corrosion rate at early stage of corrosion experiment, which is illustrated by following analysis of XRD, SEM and EDS results.

#### 3.2. Characterizations of corroded samples

XRD analysis results of T91 exposed to different  $s\text{CO}_2$  environments for 50 h and 500 h of exposure at 550 °C and 15 MPa are shown in Fig. 3. The phases of corrosion products of T91 were quite different. The surface oxide scales grown on T91 corroded in  $s\text{CO}_2$  were composed of  $\text{Fe}_3\text{O}_4$  and  $\text{Fe}_{3-x}\text{Cr}_x\text{O}_4$  spinel after 500 h exposure. Previous studies have confirmed the formation of  $\text{Fe}_3\text{O}_4$  and  $\text{Fe}_{3-x}\text{Cr}_x\text{O}_4$  spinel on Fe-based alloys with low Cr content such as VM12 [33], T22 [48], T23 [49], and T91 [20,30,31], etc. Different from corrosion products in  $s\text{CO}_2$  environment,  $\text{Fe}_2\text{O}_3$  and  $\text{FeS}$  were respectively detected on corroded T91 surface for exposure to  $s\text{CO}_2$  with  $\text{O}_2$  and to  $s\text{CO}_2$  with  $\text{H}_2\text{S}$  impurity. The different phases grown on corroded T91 surface imply that different corrosion process occurred when T91 samples were exposed to the four  $s\text{CO}_2$  environments. Interestingly, the surface corrosion product of corroded T91 in  $s\text{CO}_2$  with  $\text{SO}_2$  impurity was same as that in  $s\text{CO}_2$ . Following further characterizations would clarify this result well.

Fig. 4 shows the top-view SEM morphology of corroded T91 exposed

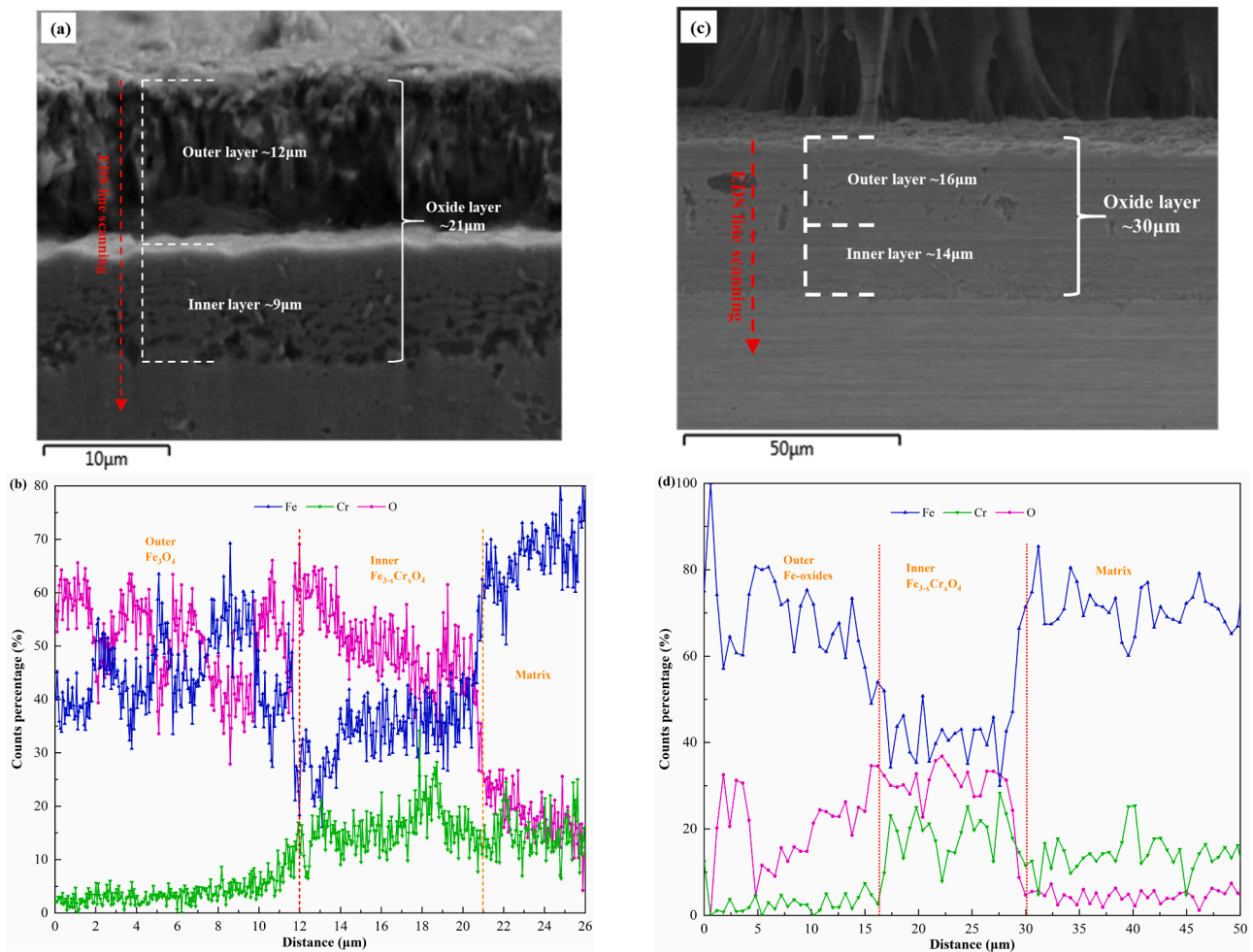


Fig. 5. Cross-sectional EDS line scanning results of T91 for exposure 500 h at 550 °C and 15 MPa. (a) and (b), pure sCO<sub>2</sub>. (c) and (d), sCO<sub>2</sub> with 100 ppm O<sub>2</sub>.

to pure sCO<sub>2</sub> and sCO<sub>2</sub> with O<sub>2</sub> impurity environments at 550 °C and 15 MPa for 50 h and 500 h. For corrosion test in pure sCO<sub>2</sub>, a great number of pores were observed on the surface oxidation film. With the exposure time prolonged, the pores were disappeared because the growth or/and further formation of oxides. As a result, some oxides nodules were formed after 500 h exposure in pure sCO<sub>2</sub>. The corrosion mechanism of T91 exposed to pure sCO<sub>2</sub> is likely to be [20,50]:



The formed oxides phases on T91 surfaces after exposed to sCO<sub>2</sub> with addition of O<sub>2</sub> impurity is different from that in pure sCO<sub>2</sub> seen in Fig. 4, indicating that the corrosion process may be changed due to the existence of O<sub>2</sub> impurity. Irregular, loose oxides phases were found after 50 h corrosion test, and the main oxides were composed of Fe<sub>2</sub>O<sub>3</sub> and Fe<sub>3</sub>O<sub>4</sub> after 500 h exposure (can be seen from XRD results in Fig. 3.), which shows a different surface morphology from Fe<sub>3</sub>O<sub>4</sub>.

To illustrate the effect of O<sub>2</sub> impurity on T91 corrosion, we have calculated the Gibbs free energy  $\Delta G^\theta$  of possible reactions at 550 °C using a commercial software HSC [51], shown in reaction (5)-(7). All the three relevant corrosion process possibly occurred in the sCO<sub>2</sub> with addition of O<sub>2</sub> impurity. The corresponding equilibrium oxygen partial pressures are respectively  $0.19 \times 10^{-27}$  MPa,  $0.3 \times 10^{-26}$  MPa and  $0.12 \times 10^{-16}$  MPa, according to  $p_{\text{O}_2} = \exp \frac{\Delta G^\theta}{RT}$  (R is the molar gas constant, and T is the temperature in Kelvin) [47]. The oxygen partial

pressure in the corrosion environment with 100 ppm O<sub>2</sub> impurity is much higher than corresponding equilibrium oxygen partial pressures. Therefore, the reaction (5) and (6) proceed to the formation of Fe oxides, and the produced Fe<sub>3</sub>O<sub>4</sub> would be further oxidized into Fe<sub>2</sub>O<sub>3</sub> with the exposure prolonged. The possible corrosion process of T91 in sCO<sub>2</sub> with additional O<sub>2</sub> impurity was that Fe atoms would be mainly oxidized into Fe<sub>3</sub>O<sub>4</sub> at the early stage of exposure, as shown in Fig. 3(a). With the corrosion prolonged, part of Fe<sub>3</sub>O<sub>4</sub> formed on corroded T91 surface would be further oxidized, leading to the formation of Fe<sub>2</sub>O<sub>3</sub> after 500 h exposure, as shown in Fig. 3(b).

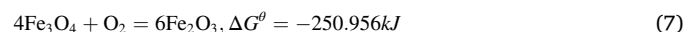
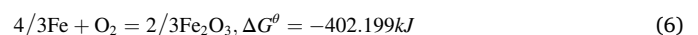
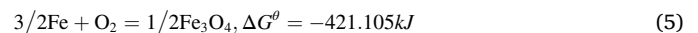


Fig. 5 shows the cross-sectional SEM images and EDS line scanning results of T91 sample exposed to pure sCO<sub>2</sub> and sCO<sub>2</sub> with 100 ppm O<sub>2</sub> at 550 °C and 15 MPa for 500 h. The micrographs of cross sections of investigated material T91 showed that the thickness of oxidation film increased with the addition of O<sub>2</sub> impurity. The oxidation thickness of corroded T91 was respectively about 21 μm and 30 μm in pure sCO<sub>2</sub> and sCO<sub>2</sub> with 100 ppm O<sub>2</sub> environments. Typical duplex-layer oxide film structures [25,29] were formed for the two types of corroded samples. The difference was that the addition of O<sub>2</sub> impurity has a positive effect on the formation of Fe<sub>2</sub>O<sub>3</sub> oxide, resulting in that the outer oxide layer was composed of Fe<sub>3</sub>O<sub>4</sub> and Fe<sub>2</sub>O<sub>3</sub>, seen from EDS line scanning results

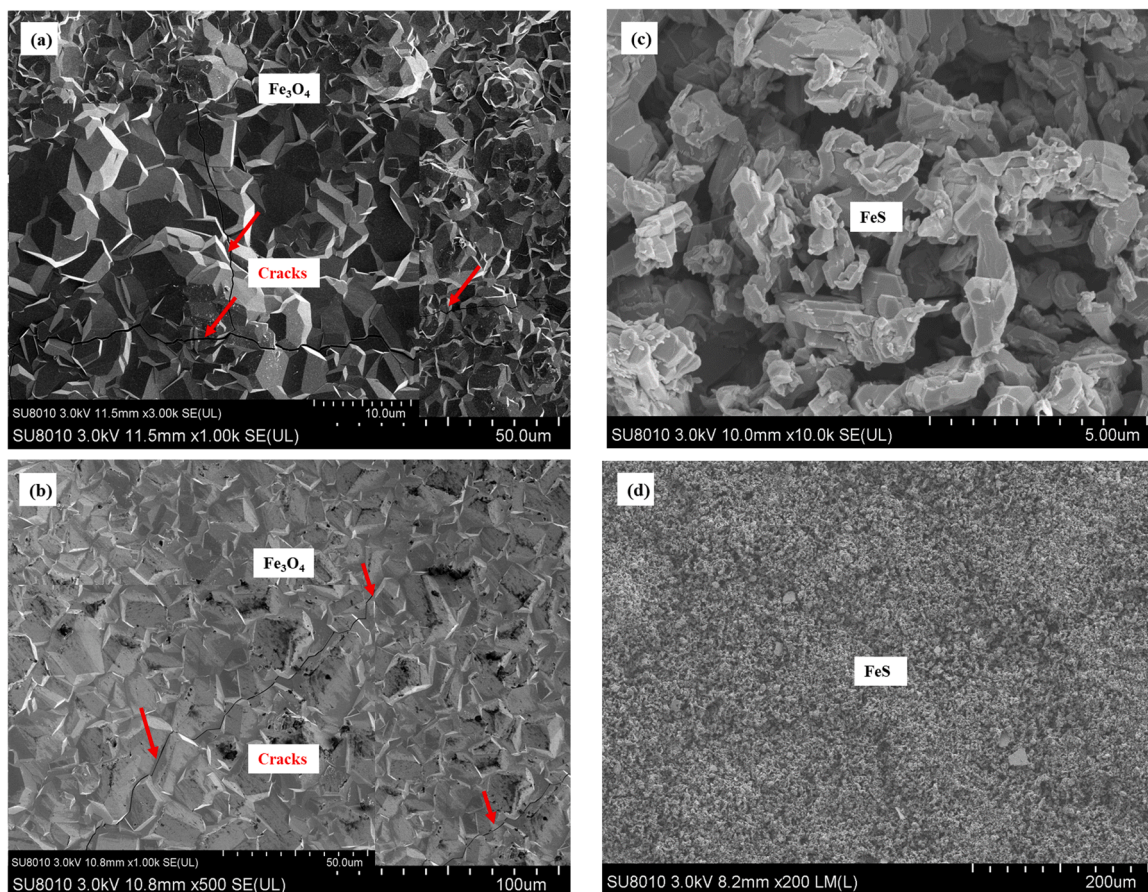


Fig. 6. Surface SEM images of T91 exposed to  $s\text{CO}_2$  with 100 ppm  $\text{SO}_2$  for (a) 50 h and (b) 500 h, and to  $s\text{CO}_2$  with 100 ppm  $\text{H}_2\text{S}$  for (c) 50 h and (d) 500 h at 550 °C and 15 MPa.

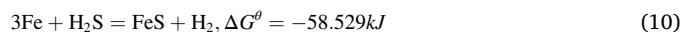
in Fig. 5. In addition,  $\text{O}_2$  impurity promoted the formation of oxides, leading to a thicker oxides layer, consistent with the mass gain results in Fig. 2. Although the introduction of  $\text{O}_2$  impurity enhanced the partial pressure of oxygen, low Cr content of T91 still could not form protective  $\text{Cr}_2\text{O}_3$  layer, in turn resulting in an accelerated corrosion rate for T91.

Surface SEM micrographs of corroded T91 exposed to pure  $s\text{CO}_2$  with 100 ppm  $\text{SO}_2$  or  $\text{H}_2\text{S}$  impurity environments at 550 °C and 15 MPa was shown in Fig. 6. It is worth noting that some cracks were observed on the surface of corroded T91 exposed to pure  $s\text{CO}_2$  with 100 ppm  $\text{SO}_2$ , which may be attributed to the rapid growth of oxides (seen in Fig. 2) and the generation of sulfur. These may cause defects and internal vulcanization and seriously affects the mechanical strength of metal materials [52–54]. In addition, additional stresses often formed during cooling or heating process as a result of the differences in the thermal expansion coefficients of the oxide layers. These stresses may also lead to cracks. Yet further characterizations are needed to confirm this. According to the XRD analysis results in Fig. 3 and SEM images in Fig. 6(a) and (b), the surface oxide film was  $\text{Fe}_3\text{O}_4$  for test in  $s\text{CO}_2$  with  $\text{SO}_2$  impurity environment. From the EDS line scanning results of cross section in Fig. 7(b), the inner layer of T91 exposed to pure  $s\text{CO}_2$  with  $\text{SO}_2$  impurity was composed of Fe-Cr spinel and FeS. As shown in Fig. 7(a), the total thickness of corrosion layer was about  $70\mu\text{m}$  with  $40\mu\text{m}$  of inner layer. Based on the characterization results and thermodynamic calculation of relevant Gibbs free energy, the corrosion mechanism with  $\text{SO}_2$  participation is likely to be:



$\text{SO}_2$  molecules similar to  $\text{CO}_2$  react with Fe atom to form  $\text{Fe}_3\text{O}_4$  (reaction (8)) at the initial corrosion stage, and the reaction (2) would occur at the same time to form  $\text{Fe}_3\text{O}_4$ . The  $\text{CO}_2/\text{CO}$  and  $\text{S}_2/\text{SO}_2$  would transport to the oxides-matrix interface, producing  $\text{Fe}_{3-x}\text{Cr}_x\text{O}_4$  (reaction 4) spinel and FeS (reaction 9) [43].

For corrosion test in pure  $s\text{CO}_2$  with 100 ppm  $\text{H}_2\text{S}$ , based on SEM results in Fig. 6 and EDS line scanning of corrosion layer in Fig. 7(c) and (d), FeS is the main phase in the outer corrosion layer with a thickness of about  $80\mu\text{m}$ , very different from the corrosion products when exposed to pure  $s\text{CO}_2$  with/without 100 ppm  $\text{SO}_2$  or  $\text{O}_2$  impurity. The corresponding reaction (10) is shown as follows. Additionally,  $\text{CO}_2$  molecules pass through the loose sulfide as well and participate in reaction (4), forming inner Fe-Cr spinel. Considering thermodynamic stability,  $\text{CO}_2$  with 100 ppm  $\text{H}_2\text{S}$  at 550 °C and 15 MPa has an equilibrium  $p_{\text{O}_2}$  of  $1.8 \times 10^{-20}$  MPa and  $p_{\text{S}_2}$  of  $7.2 \times 10^{-4}$  MPa, calculated using thermodynamic software. As shown in Fig. 8, the equilibrium gas composition was close to the interface of iron sulfide and iron oxide in terms of the thermodynamically stable reaction product. Hence, the observed two-layer sulfide/oxide in our experiment was consistent with thermodynamic considerations.



In order to determine the effect of impurities on carburization behaviors of T91 exposed to  $s\text{CO}_2$  environments at 550 °C and 15 MPa, we etched the sample cross-sections using Murakami's Reagent to reveal carbides. The etchant preparation and etching process are consistent with the method provided in reference [46] except that the samples were immersed in the heated etchant for times ranging from 60 s to 90 s. Metal carbides areas were measured using ImageJ software, and the results are shown in Fig. 9. The decreased fractions of carburization area

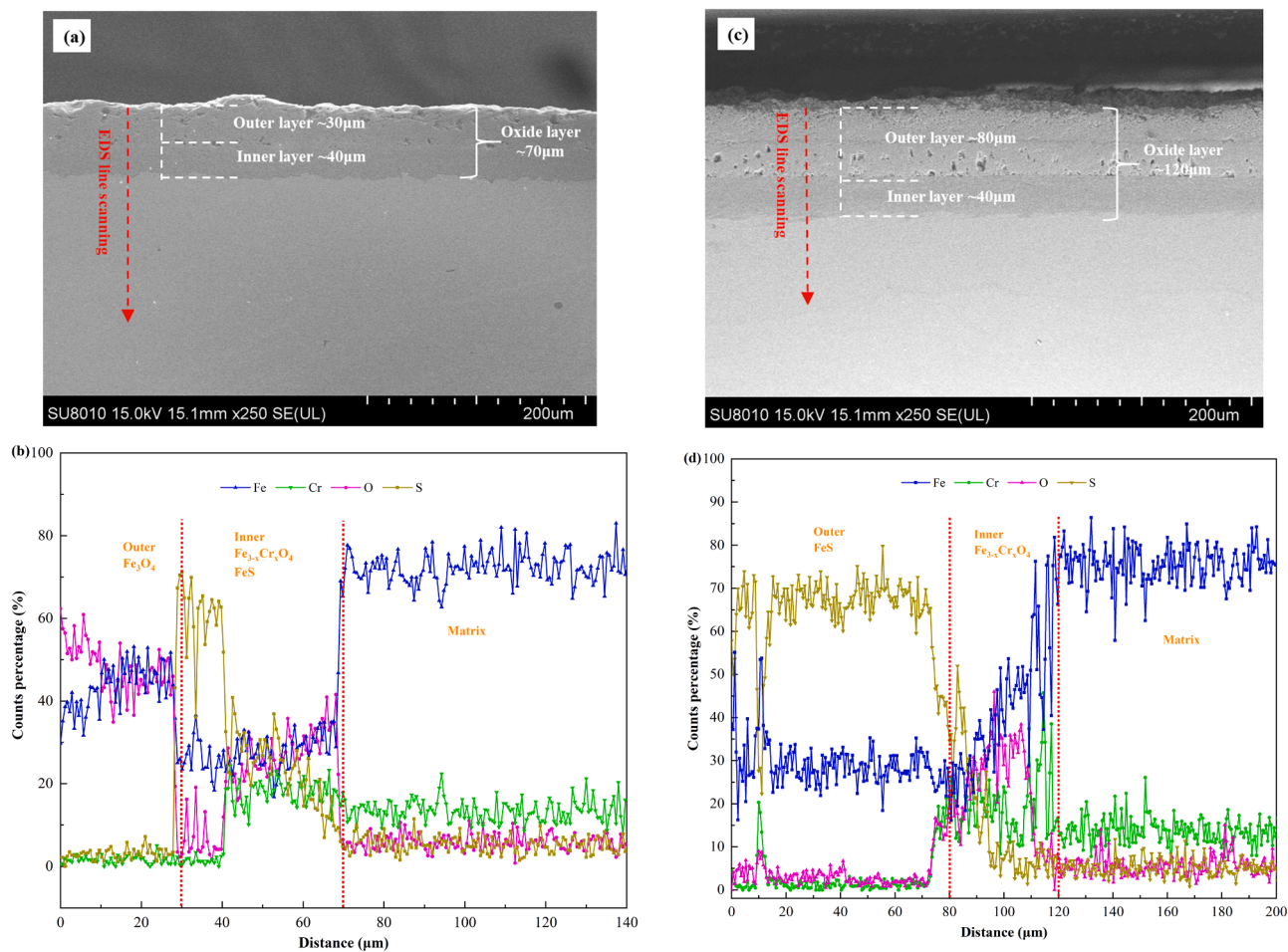


Fig. 7. Cross-sectional EDS line scanning results of T91 for exposure 500 h at 550 °C and 15 MPa. (a) and (b), sCO<sub>2</sub> with 100 ppm SO<sub>2</sub>. (c) and (d), sCO<sub>2</sub> with 100 ppm H<sub>2</sub>S.

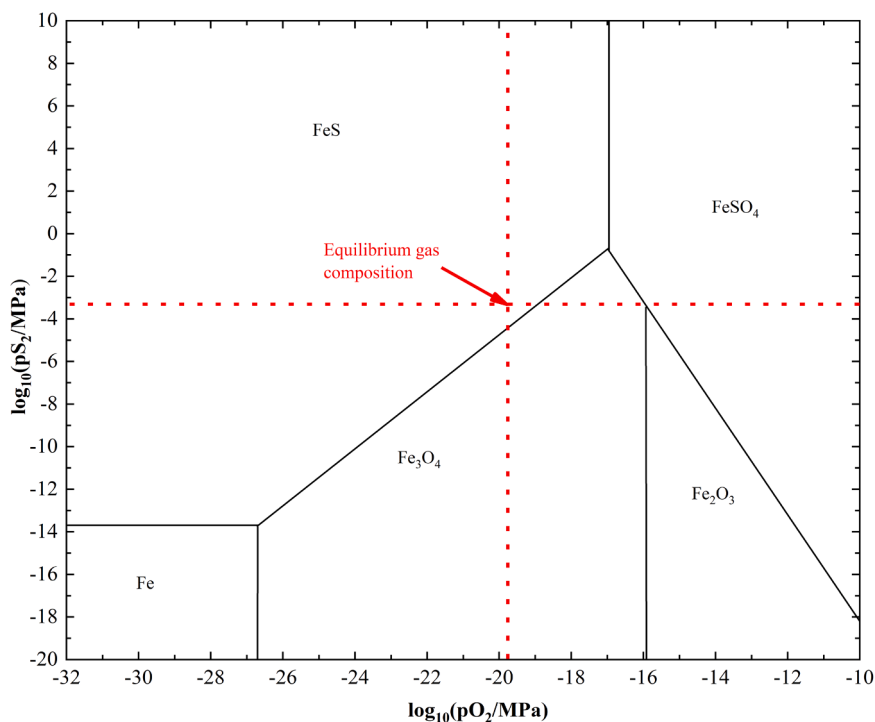


Fig. 8. Thermochemical diagrams calculated using HSC software for 550 °C and 15 MPa in the Fe-S-O system.

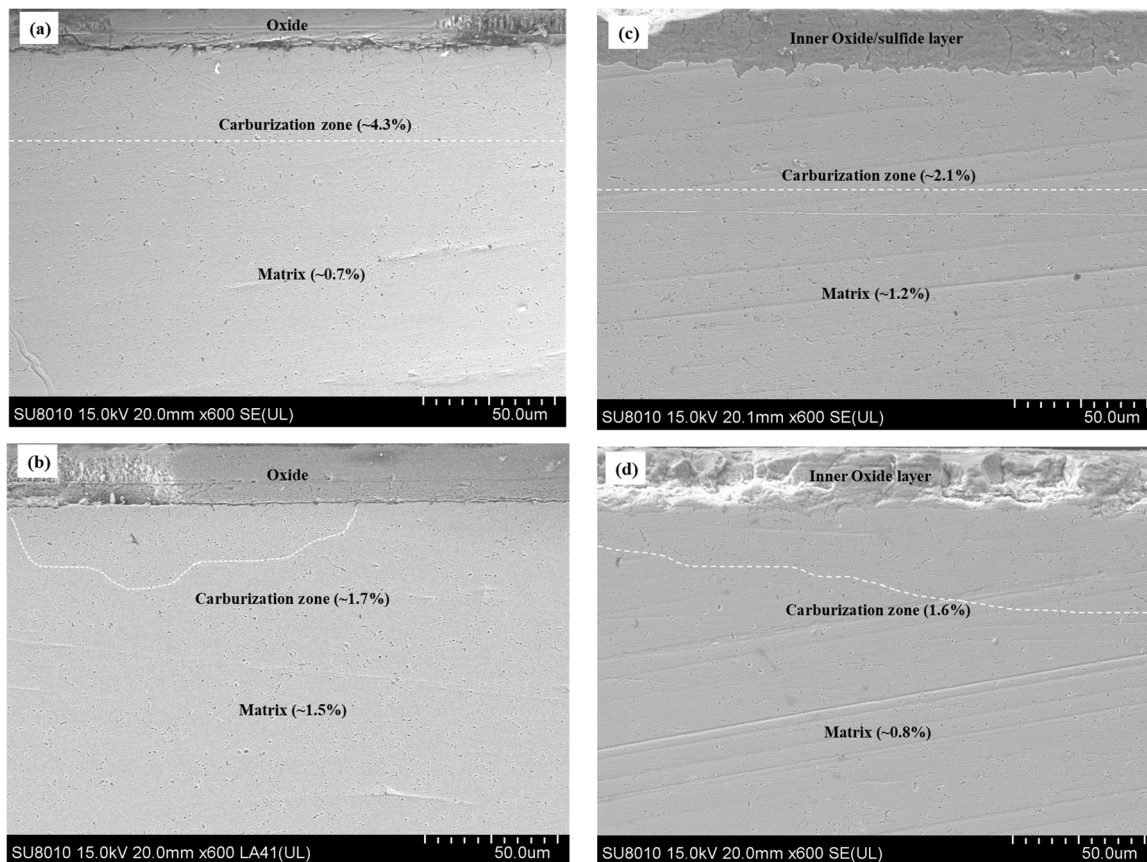


Fig. 9. Cross-sectional SEM images of etched T91 samples exposed to (a) sCO<sub>2</sub>, (b) sCO<sub>2</sub> with 100 ppm O<sub>2</sub>, (c) sCO<sub>2</sub> with 100 ppm SO<sub>2</sub> and (d) sCO<sub>2</sub> with 100 ppm H<sub>2</sub>S at 550 °C and 15 MPa for 250 h. And percentages represent the measured fractions of carbides areas using ImageJ software.

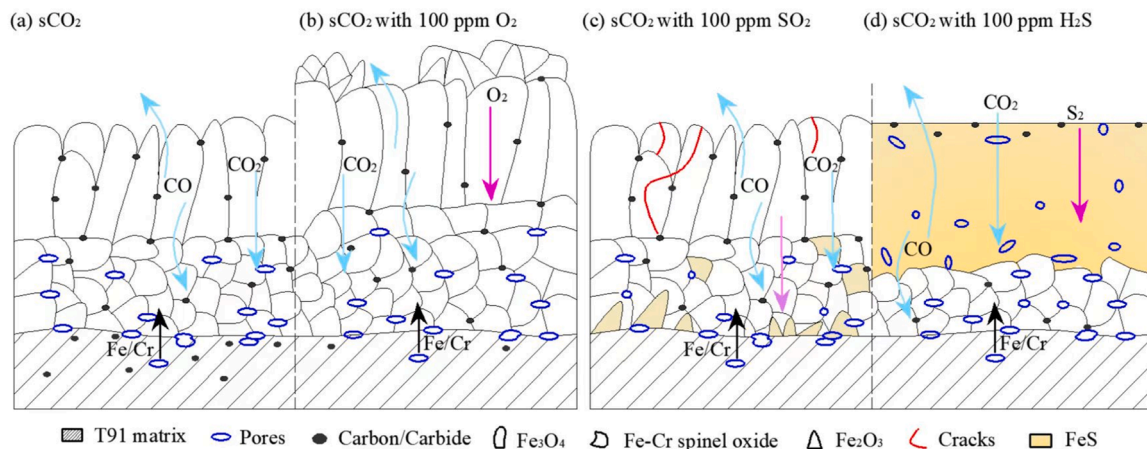


Fig. 10. Schematic illustrations of corrosion mechanisms for T91 when exposed to different sCO<sub>2</sub> environments at 550 °C and 15 MPa. (a) pure sCO<sub>2</sub>, and sCO<sub>2</sub> with O<sub>2</sub> impurity, (b) sCO<sub>2</sub> with SO<sub>2</sub> or H<sub>2</sub>S impurity.

at 550 °C resulting from the presence of O<sub>2</sub>, SO<sub>2</sub> or H<sub>2</sub>S were observed after the etching experiment. As shown in Fig. 9(b), little or no carburization occurred in pure sCO<sub>2</sub> with O<sub>2</sub> impurity for 250 h of exposure. It can be proposed that the presence of O<sub>2</sub> could reduce the carbon activity in the gas with a higher oxygen partial pressure, resulting in less inwards penetration of CO/CO<sub>2</sub> to form carbides in the alloy beneath the oxide. According to the results in Fig. 9(c) and (d), we can find that both SO<sub>2</sub> and H<sub>2</sub>S could improve carburization resistance of the alloy, consistent with previous studies [44,46]. The explanation would be that sulfur species in sCO<sub>2</sub> can inhibit carbon species from reaching the alloy,

probably through a competitive adsorption process.

Fig. 10 shows the schematic illustrations of the corrosion behaviors of T91 when exposed to four different sCO<sub>2</sub> environments at 550 °C and 15 MPa. For corrosion test in pure sCO<sub>2</sub>, shown in Fig. 10(a), the corrosion process started with the adsorption of CO<sub>2</sub> molecules, formed metal oxides by reaction (2 and 3). Part of the generated CO would escape into the environment, forming carbon deposition on the surface of material by Boudouard reaction [25]. Some CO molecules penetrated into the matrix-oxides interface zone, produced carbon deposition area by reaction (3). The CO<sub>2</sub> and generated CO reacted with a large amount

of Fe atoms to form magnetite. As a result, a number of vacancies formed, which provided channels for CO<sub>2</sub> to form inner Fe-Cr spinel oxide, according to the reaction (4). As shown in Fig. 10(b), With the addition of O<sub>2</sub> impurity, O<sub>2</sub> molecules react directly with Fe atoms to form Fe<sub>2</sub>O<sub>3</sub> and Fe<sub>3</sub>O<sub>4</sub>, and part of Fe<sub>3</sub>O<sub>4</sub> would be further oxidized to Fe<sub>2</sub>O<sub>3</sub>. At the same time, some CO<sub>2</sub> molecules passed through the oxides, reached at the oxides-matrix interface and reacted with surrounding elements to form Fe-Cr spinel inner oxide according to the reaction (4). The presence of O<sub>2</sub> impurity would restrict the carbon activity in the gas to improve carburization resistance as a result of the enhanced oxygen partial pressure.

When the sCO<sub>2</sub> environment contains impurities with sulfur element like SO<sub>2</sub> and H<sub>2</sub>S, based on the results of this study and the thermodynamic calculation, SO<sub>2</sub> would react with Fe atoms to form Fe<sub>3</sub>O<sub>4</sub> by reaction (8), which was similar to CO<sub>2</sub> oxidation process. With the corrosion test prolonged, the produced sulfurs ingress into the matrix-oxides interface and react with Fe atoms forming internal FeS by reaction (9). Rapid corrosion rate, internal sulfides growth and thermal stresses in sCO<sub>2</sub> with SO<sub>2</sub> impurity may lead to the formation of cracks on the surface of the investigated material, as shown in Fig. 10(c). For corrosion test in sCO<sub>2</sub> with introduction of H<sub>2</sub>S impurity, H<sub>2</sub>S (sulfur mostly exists in the form of SO<sub>2</sub>) caused the formation of FeS according to reaction (10), shown in Fig. 10(d). Similarly, CO<sub>2</sub> molecules passed through the loose sulfide layer and participate in reaction (4), forming inner Fe-Cr spinel. SO<sub>2</sub> or H<sub>2</sub>S existed in sCO<sub>2</sub> environment could reduce the degree of carburization because of a competitive adsorption process between carbon and sulfur species.

#### 4. Conclusion

- (1) The corrosion kinetics of heat resistant T91 in sCO<sub>2</sub> environment and sCO<sub>2</sub> with 100 ppm O<sub>2</sub> impurity at 550 °C and 15 MPa exhibited a near parabolic behavior, indicating that the oxidation process was controlled by ion diffusion. Addition of SO<sub>2</sub> and H<sub>2</sub>S impurity remarkably increased mass gains, while the effect of O<sub>2</sub> impurity on corrosion mass changes was slighter.
- (2) After 500 h exposure to different sCO<sub>2</sub> environments, a duplex-layer oxide or sulfide scale was formed on the surface of experiment material. For corrosion in pure sCO<sub>2</sub> environment, typical external magnetite and internal Fe-Cr spinel layer were formed. While Fe<sub>2</sub>O<sub>3</sub> phase was generated in outer corrosion layer due to enhanced partial pressure of oxygen. The oxidation thickness of corroded T91 was respectively about 21 μm and 30 μm after exposure to pure sCO<sub>2</sub> and sCO<sub>2</sub> with 100 ppm O<sub>2</sub> environments for 500 h.
- (3) With additional SO<sub>2</sub> or H<sub>2</sub>S impurity, a new corrosion product, FeS, were observed on T91 surface. Moreover, the thickness of corrosion layer increased to about 70 μm and 120 μm for exposure to sCO<sub>2</sub> with SO<sub>2</sub> or H<sub>2</sub>S impurity, respectively. Rapid corrosion rate, internal FeS growth and thermal stresses may lead to the formation of cracks on material surface when exposed to pure sCO<sub>2</sub> with SO<sub>2</sub> impurity. While different from SO<sub>2</sub> impurity, H<sub>2</sub>S additions caused an outer FeS corrosion layer.
- (4) Introduction of all the three impurities can reduce the degree of carburization of the alloy, as a result of a restricted carbon activity in the gas or a competitive adsorption process between carbon and sulfur species.

#### CRedit authorship contribution statement

**Yafei Liu:** Methodology, Investigation, Experiments, Visualization, Writing – original draft, Writing – review & editing. **Gang Xiao:** Methodology, Writing – review & editing, Funding acquisition, Project administration, Supervision. **Mingxuan Wang:** Conceptualization, Methodology, Investigation, Experiments. **Qinghe Guo:** Investigation, Experiments, Writing – review & editing. **Zheng Wang:** Methodology,

Experiments. **Yi Wu:** Experiments. **Haoran Xu:** Writing – review & editing, Supervision. **Dong Chen:** Resources, Supervision.

#### Declaration of Competing Interest

The authors declare that they have no known competing financial interests or personal relationships that could have appeared to influence the work reported in this paper.

#### Data availability

Data will be made available on request.

#### Acknowledgments

This work was supported by the Key R&D Program of Zhejiang (NO. 2022C01043); the Zhejiang Provincial Natural Science Foundation (NO. LR20E060001); and the Fundamental Research Funds for the Central Universities (2022ZFJH004). Authors also thanks Mrs. Na Zheng at State Key Laboratory of Chemical Engineering in Zhejiang University for Performing SEM and EDS.

#### References

- [1] Y. Ming, K. Liu, F. Zhao, H. Fang, S. Tan, R. Tian, Dynamic modeling and validation of the 5 MW small modular supercritical CO<sub>2</sub> Brayton-Cycle reactor system, *Energy Conv. Manag.* 253 (2022), 115184, <https://doi.org/10.1016/j.enconman.2021.115184>.
- [2] D. Milani, M.T. Luu, R. McNaughton, A. Abbas, A comparative study of solar heliostat assisted supercritical CO<sub>2</sub> recompression Brayton cycles: dynamic modelling and control strategies, *J. Supercrit. Fluids* 120 (2017) 113–124, <https://doi.org/10.1016/j.supflu.2016.09.009>.
- [3] Z. Guo, Y. Zhao, Y. Zhu, F. Niu, D. Lu, Optimal design of supercritical CO<sub>2</sub> power cycle for next generation nuclear power conversion systems, *Prog. Nucl. Energy* 108 (2018) 111–121, <https://doi.org/10.1016/j.pnucene.2018.04.023>.
- [4] M. Li, H. Zhu, J. Guo, K. Wang, W. Tao, The development technology and applications of supercritical CO<sub>2</sub> power cycle in nuclear energy, solar energy and other energy industries, *Appl. Therm. Eng.* 126 (2017) 255–275, <https://doi.org/10.1016/j.pnucene.2018.04.023>.
- [5] S. Park, J. Kim, M. Yoon, D. Rhim, C. Yeom, Thermodynamic and economic investigation of coal-fired power plant combined with various supercritical CO<sub>2</sub> Brayton power cycle, *Appl. Therm. Eng.* 130 (2018) 611–623, <https://doi.org/10.1016/j.applthermaleng.2017.10.145>.
- [6] W. Bai, Y. Zhang, Y. Yang, H. Li, M. Yao, 300 MW boiler design study for coal-fired supercritical CO<sub>2</sub> Brayton cycle, *Appl. Therm. Eng.* 135 (2018) 66–73, <https://doi.org/10.1016/j.applthermaleng.2018.01.110>.
- [7] P. Garg, P. Kumar, K. Srinivasan, Supercritical carbon dioxide Brayton cycle for concentrated solar power, *J. Supercrit. Fluids* 76 (2013) 54–60, <https://doi.org/10.1016/j.supflu.2013.01.010>.
- [8] S. Khatoun, M.H. Kim, Preliminary design and assessment of concentrated solar power plant using supercritical carbon dioxide Brayton cycles, *Energy Conv. Manag.* 252 (2022), 115066, <https://doi.org/10.1016/j.enconman.2021.115066>.
- [9] Y. Liang, J. Chen, Z. Yang, J. Chen, X. Luo, Y. Chen, Economic-environmental evaluation and multi-objective optimization of supercritical CO<sub>2</sub> based-central tower concentrated solar power system with thermal storage, *Energy Conv. Manag.* 238 (2021), 114140, <https://doi.org/10.1016/j.enconman.2021.114140>.
- [10] S.A. Wright, R.F. Radcliff, M.E. Vernon, G.E. Rochau, P.S. Pickard, Operation and analysis of a supercritical CO<sub>2</sub> Brayton cycle, SAND2010-0171, Sandia Rep. (2010), <https://doi.org/10.2172/984129>.
- [11] J. Pasch, M. Carlson, D. Fleming, G. Rochau, Evaluation of recent data from the SANDIA national laboratories closed Brayton cycle testing, No.GT2016-57620, Turbo Expo: Power Land, Sea, Air (2016), <https://doi.org/10.1115/GT2016-57620>.
- [12] E.M. Clementoni, T.L. Cox, M.A. King, Off-nominal component performance in a supercritical carbon dioxide Brayton cycle, *J. Eng. Gas. Turbines Power* 138 (2016), 011703, <https://doi.org/10.1115/1.4031182>.
- [13] E.M. Clementoni, T.L. Cox, Practical aspects of supercritical carbon dioxide Brayton system testing, *Proc. 4th Int. Symp. ., Pittsburgh, Pa.* (2014).
- [14] X. Fan, Y. Wang, Y. Zhou, J. Chen, Y. Huang, J. Wang, Experimental study of supercritical CO<sub>2</sub> leakage behavior from pressurized vessels, *Energy* 150 (2018) 342–350, <https://doi.org/10.1016/j.energy.2018.02.147>.
- [15] H. Zhao, Q. Deng, W. Huang, D. Wang, Z. Feng, Thermodynamic and economic analysis and multi-objective optimization of supercritical CO<sub>2</sub> Brayton cycles, *J. Eng. Gas. Turbines Power* 138 (2016), 081602, <https://doi.org/10.1115/1.4032666>.
- [16] G. Manente, F.M. Fortuna, Supercritical CO<sub>2</sub> power cycles for waste heat recovery: a systematic comparison between traditional and novel layouts with dual expansion, *Energy Conv. Manag.* 197 (2019), 111777, <https://doi.org/10.1016/j.enconman.2019.111777>.

- [17] G.R. Holcomb, C. Carney, Ö.N. Doğan, Oxidation of alloys for energy applications in supercritical CO<sub>2</sub> and H<sub>2</sub>O, *Corros. Sci.* 109 (2016) 22–35, <https://doi.org/10.1016/j.corsci.2016.03.018>.
- [18] H.J. Lee, H. Kim, S.H. Kim, C. Jang, Corrosion and carburization behavior of chromia-forming heat resistant alloys in a high-temperature supercritical-carbon dioxide environment, *Corros. Sci.* 99 (2015) 227–239, <https://doi.org/10.1016/j.corsci.2015.07.007>.
- [19] H.J. Lee, G.O. Subramanian, S.H. Kim, C. Jang, Effect of pressure on the corrosion and carburization behavior of chromia-forming heat-resistant alloys in high-temperature carbon dioxide environments, *Corros. Sci.* 111 (2016) 649–658, <https://doi.org/10.1016/j.corsci.2016.06.004>.
- [20] H. Yang, W. Liu, B. Gong, E. Jiang, Y. Huang, G. Zhang, Y. Zhao, Corrosion behavior of typical structural steels in 500°C, 600°C and high pressure supercritical carbon dioxide conditions, *Corros. Sci.* 192 (2021), 109801, <https://doi.org/10.1016/j.corsci.2021.109801>.
- [21] M.H.S. Bidabadi, Y. Zheng, A. Rehman, L. Yang, C. Zhang, H. Chen, Z.G. Yang, Effect of CO<sub>2</sub> gas pressure on composition, growth rate, and structure of duplex oxide formed on 9Cr steel at 550°C, *Corros. Sci.* 163 (2020), 108252, <https://doi.org/10.1016/j.corsci.2019.108252>.
- [22] B.A. Pint, J.R. Keiser, The effect of temperature and pressure on supercritical CO<sub>2</sub> compatibility of conventional structural alloys, Oak Ridge Natl. Lab, Oak Ridge, U. S. (2016).
- [23] F. Rouillard, T. Furukawa, Corrosion of 9-12Cr ferritic–martensitic steels in high-temperature CO<sub>2</sub>, *Corros. Sci.* 105 (2016) 120–132, <https://doi.org/10.1016/j.corsci.2016.01.009>.
- [24] X. Guo, Z. Liu, L. Li, J. Cheng, H. Su, L. Zhang, Revealing the long-term oxidation and carburization mechanism of 310S SS and Alloy 800H exposed to supercritical carbon dioxide, *Mater. Charact.* 183 (2022), 111603, <https://doi.org/10.1016/j.matchar.2021.111603>.
- [25] F. Rouillard, G. Moine, L. Martinelli, J.C. Ruiz, Corrosion of 9Cr steel in CO<sub>2</sub> at intermediate temperature I: mechanism of void-induced duplex oxide formation, *Oxid. Met.* 77 (2012) 27–55, <https://doi.org/10.1007/s11085-011-9271-5>.
- [26] F. Rouillard, G. Moine, L. Martinelli, J.C. Ruiz, Corrosion of 9Cr steel in CO<sub>2</sub> at intermediate temperature II: mechanism of carburization, *Oxid. Met.* 77 (2012) 57–70, <https://doi.org/10.1007/s11085-011-9272-4>.
- [27] F. Rouillard, L. Martinelli, Corrosion of 9Cr steel in CO<sub>2</sub> at intermediate temperature III: Modelling and simulation of void-induced duplex oxide growth, *Oxid. Met.* 77 (2012) 71–83, <https://doi.org/10.1007/s11085-011-9273-3>.
- [28] D.R. Holmes, D. Mortimer, J. Newell, Discovery and assessment of accelerated corrosion in Fe-9Cr alloys and steels, *Proc. Br. Nucl. Energy Soc. Int. Conf., U. Kingd.* (1974).
- [29] H. Chen, S.H. Kim, C. Kim, J. Chen, C. Jang, Corrosion behaviors of four stainless steels with similar chromium content in supercritical carbon dioxide environment at 650°C, *Corros. Sci.* 156 (2019) 16–31, <https://doi.org/10.1016/j.corsci.2019.04.043>.
- [30] Y. Gui, Z. Liang, Q. Zhao, Corrosion and carburization behavior of heat-resistant steels in a high-temperature supercritical carbon dioxide environment, *Oxid. Met.* 92 (2019) 123–136, <https://doi.org/10.1007/s11085-019-09917-x>.
- [31] Z. Liang, Y. Gui, Y. Wang, Q. Zhao, Corrosion performance of heat-resisting steels and alloys in supercritical carbon dioxide at 650°C and 15 MPa, *Energy* 175 (2019) 345–352, <https://doi.org/10.1016/j.energy.2019.03.014>.
- [32] Z. Liang, Y. Gui, Y. Wang, Q. Zhao, High-temperature corrosion resistance of nickel-base alloy 617 in supercritical carbon dioxide environment, *Mater. Res. Express* 7 (2020), 016548, <https://doi.org/10.1088/2053-1591/ab6388>.
- [33] Y. Gui, Z. Liang, H. Shao, Q. Zhao, Corrosion behavior and lifetime prediction of VM12, Sanicro 25 and Inconel 617 in supercritical carbon dioxide at 600°C, *Corros. Sci.* 175 (2020), 108870, <https://doi.org/10.1016/j.corsci.2020.108870>.
- [34] T. Gheno, D. Monceau, J. Zhang, D.J. Young, Carburisation of ferritic Fe–Cr alloys by low carbon activity gases, *Corros. Sci.* 53 (2011) 2767–2777, <https://doi.org/10.1016/j.corsci.2011.05.013>.
- [35] D.J. Young, T.D. Nguyen, P. Felfer, J. Zhang, J.M. Cairney, Penetration of protective chromia scales by carbon, *Scr. Mater.* 77 (2014) 29–32, <https://doi.org/10.1016/j.scriptamat.2014.01.009>.
- [36] D. Young, P. Huczowski, T. Olszewski, T. Hüttel, L. Singheiser, W.J. Quadackers, Non-steady state carburisation of martensitic 9–12% Cr steels in CO<sub>2</sub> rich gases at 550°C, *Corros. Sci.* 88 (2014) 161–169, <https://doi.org/10.1016/j.corsci.2014.07.024>.
- [37] R.P. Oleksak, F. Rouillard, Materials performance in CO<sub>2</sub> and supercritical CO<sub>2</sub>, in: R.J.M. Konings, R.E. Stoller (Eds.), *Comprehensive Nuclear Materials*, 2nd edition., Elsevier, Oxford, 2020, pp. 422–CO451, <https://doi.org/10.1016/B978-0-12-803581-8.11622-4>.
- [38] J. Mahaffey, D. Adam, A. Brittan, M. Anderson, K. Sridharan, Corrosion of alloy haynes 230 in high temperature supercritical carbon dioxide with oxygen impurity additions, *Oxid. Met.* 86 (2016) 567–580, <https://doi.org/10.1007/s11085-016-9654-8>.
- [39] J. Mahaffey, A. Schroeder, D. Adam, A. Brittan, M. Anderson, A. Couet, K. Sridharan, Effects of CO and O<sub>2</sub> impurities on supercritical CO<sub>2</sub> corrosion of alloy 625, *Metall. Mater. Trans. A* 49 (2018) 3703–3714, <https://doi.org/10.1007/s11661-018-4727-8>.
- [40] K. Li, Y. Zeng, J.L. Luo, Corrosion of SS310 and Alloy 740 in high temperature supercritical CO<sub>2</sub> with impurities H<sub>2</sub>O and O<sub>2</sub>, *Corros. Sci.* 184 (2021), 109350, <https://doi.org/10.1016/j.corsci.2021.109350>.
- [41] R.P. Oleksak, J.H. Tylczak, G.R. Holcomb, Ö.N. Doğan, High temperature oxidation of steels in CO<sub>2</sub> containing impurities, *Corros. Sci.* 164 (2020), 108316, <https://doi.org/10.1016/j.corsci.2019.108316>.
- [42] T. Gheno, D. Monceau, J. Zhang, D.J. Young, Carburisation of ferritic Fe–Cr alloys by low carbon activity gases, *Corros. Sci.* 53 (2011) 2767–2777, <https://doi.org/10.1016/j.corsci.2011.05.013>.
- [43] K. Chandra, A. Kranzmann, R.S. Neumann, F. Rizzo, Comparative study on high temperature oxidation of T92 steel in dry and wet oxyfuel environments, *Oxid. Met.* 84 (2015) 463–490, <https://doi.org/10.1007/s11085-015-9565-0>.
- [44] P. Huczowski, D.J. Young, T. Olszewski, A. Chyrkin, W.J. Quadackers, Effect of sulphur on the oxidation behaviour of possible construction materials for heat exchangers in oxyfuel plants in the temperature range 550–700°C, *Oxid. Met.* 89 (2018) 651–681, <https://doi.org/10.1007/s11085-017-9809-2>.
- [45] R.P. Oleksak, J.H. Tylczak, C.S. Carney, G.R. Holcomb, Ö.N. Doğan, High-temperature oxidation of commercial alloys in supercritical CO<sub>2</sub> and related power cycle environments, *Jom* 70 (2018) 1527–1534, <https://doi.org/10.1007/s11837-018-2952-7>.
- [46] R.P. Oleksak, J.H. Tylczak, Ö.N. Doğan, Temperature-dependence of oxidation and carburization of Grade 91 steel in CO<sub>2</sub> containing impurities, *Corro. Sci* 198 (2022), 110147, <https://doi.org/10.1007/s11837-018-2952-7>.
- [47] N. Birks, G.H. Meier, F.S. Pettit. Introduction to the high temperature oxidation of metals, Second ed., Cambridge university press., United Kingdom, 2006.
- [48] Z. Zhu, Y. Cheng, B. Xiao, H.I. Khan, H. Xu, N. Zhang, Corrosion behavior of ferritic and ferritic-martensitic steels in supercritical carbon dioxide, *Energy* 175 (2019) 1075–1084, <https://doi.org/10.1016/j.energy.2019.03.146>.
- [49] R.T. Li, B. Xiao, X. Liu, Z.L. Zhu, Y. Cheng, J.W. Li, J.Y. Cao, H.M. Ding, N. Q. Zhang, Corrosion behavior of low alloy heat-resistant steel t23 in high-temperature supercritical carbon dioxide, *J. Chin. Soc. Corr. Pro* 41 (2021) 327–334, <https://doi.org/10.11902/1005.4537.2020.115>.
- [50] F. Rouillard, F. Charton, G. Moine, Corrosion behavior of different metallic materials in supercritical carbon dioxide at 550°C and 250 bars, *Corrosion* 67 (2011), 095001, <https://doi.org/10.5006/1.3628683>.
- [51] A. Roine, Chemical reactions and Equilibrium software with extensive thermochemical database and Flowsheet simulation, HSC Chemistry 6.0. Outokumpu Technology, Pori, Finland, 2006.
- [52] Q.X. Zhao, Z. Zhang, D. Cheng, Y.G. Wang, X. Deng, High temperature corrosion of water wall materials T23 and T24 in simulated furnace atmospheres, *Chin. J. Chem. Eng.* 20 (2012) 814–822, [https://doi.org/10.1016/S1004-9541\(11\)60252-8](https://doi.org/10.1016/S1004-9541(11)60252-8).
- [53] S. Mrowec, K. Przybylski, Defect and transport properties of sulfides and sulfidation of metals, *High. Temp. Mater. Process* 6 (1984) 1–80, <https://doi.org/10.1515/HTMP.1984.6.1-2.1>.
- [54] S. Mrowec, K. Przybylski, Transport properties of sulfide scales and sulfidation of metals and alloys, *Oxid. Met.* 23 (1985) 107–139, <https://doi.org/10.1007/BF00659899>.